ADVANCED ELECTRONIC MATERIALS
www.advelectronicmat.de

# Low-Temperature Atomic Layer Deposition of High-*k* $SbO_x$ for Thin Film Transistors

*Jun Yang, Amin Bahrami,* Xingwei Ding, Panpan Zhao, Shiyang He, Sebastian Lehmann, Mikko Laitinen, Jaakko Julin, Mikko Kivekäs, Timo Sajavaara, and Kornelius Nielsch**

**$SbO_x$ thin films are deposited by atomic layer deposition (ALD) using $SbCl_5$ and $Sb(NMe_2)_3$ as antimony reactants and $H_2O$ and $H_2O_2$ as oxidizers at low temperatures. SbCl5 can react with both oxidizers, while no deposition is found to occur using $Sb(NMe_2)_3$ and $H_2O$. For the first time, the reaction mechanism and dielectric properties of ALD-$SbO_x$ thin films are systematically studied, which exhibit a high breakdown field of ≈4 MV cm$^{-1}$ and high areal capacitance ranging from 150 to 200 nF cm$^{-2}$, corresponding to a dielectric constant ranging from 10 to 13. The ZnO semiconductor layer is integrated into a $SbO_x$ dielectric layer, and thin film transistors (TFTs) are successfully fabricated. A TFT with a $SbO_x$ dielectric layer deposited at 200 °C from $Sb(NMe_2)_3$ and $H_2O_2$ presents excellent performance, such as a field effect mobility ($\mu$) of 12.4 cm$^2$ V$^{-1}$ s$^{-1}$, $I_{on}/I_{off}$ ratio of $4 \times 10^8$, subthreshold swing of 0.22 V dec$^{-1}$, and a trapping state ($N_{trap}$) of $1.1 \times 10^{12}$ eV$^{-1}$ cm$^{-2}$. The amorphous structure and high areal capacitance of $SbO_x$ boosts the interface between the semiconductor and dielectric layer of TFT devices and provide a strong electric field for electrons to improve the device mobility.**

## 1. Introduction

There has been a substantial increase in the number of studies focused on metal oxide thin films due to their enormous potential for applications, either as insulators or semiconductors.[1,2] To date, thin film transistors (TFTs) based on oxide thin films have been studied because of their excellent electrical properties, high uniformity, and good transparency.[3] With the growing need for high-performance electronics, conventional low-*k* materials such as $SiO_2$ are unable to fulfill demand due to direct tunneling, resulting in significant device reliability issues.[4] According to the generalized equation for the capacitance, $C = \varepsilon_0\varepsilon_r S/d$, where $\varepsilon_0$, $\varepsilon_r$, $S$, and $d$ are the dielectric constant of free space, relative dielectric constant, area, and thickness of the dielectric, respectively, a high-*k* dielectric material would be capable of providing strong capacitive coupling while also being scaled down to device size (below 100 nm).[5] Furthermore, the higher capacitance of a high-*k* dielectric permits sufficient charge injection into the TFT semiconductor layer and boosts the device performance. Over the last decade, various dielectrics with high-*k* values (>9), such as zirconium dioxide ($ZrO_2$), aluminum oxide ($Al_2O_3$), hafnium oxide ($HfO_2$), neodymium oxide ($Nd_2O_3$), and yttrium oxide ($Y_2O_3$), have been investigated as prospective candidates to replace the conventional dielectric $SiO_2$ gate in TFTs (**Figure 1**). $Al_2O_3$ was one of the first systems that has been studied as a substitute to $SiO_2$ as a gate dielectric. The larger bandgap of $Al_2O_3$ makes it compatible with the complementary metal–oxide–semiconductor structure.[6] In addition, Hf-based dielectrics have been proposed as promising materials for application in large-scale integrations. In 2007, Intel announced that Hf-based high-*k* materials will be used in 45 nm manufacturing, which is the first high-*k* material commercial production in the world.[7] Furthermore, Zeumault and Subramanian reported that the mobility of ZnO TFTs can be strongly improved by using $ZrO_2$ as a booster gate dielectric via a thermally activated emissive process.[8] However, to date, the number of high-*k* dielectrics is still limited and new high-*k* material candidates still need to be further developed. Recently, antimony oxide was reported as a new dielectric material due to its good

J. Yang, A. Bahrami, P. Zhao, S. He, S. Lehmann, K. Nielsch
Institute for Metallic Materials
Leibniz Institute of Solid State and Materials Science
01069 Dresden, Germany
E-mail: a.bahrami@ifw-dresden.de; k.nielsch@ifw-dresden.de
J. Yang, P. Zhao, S. He, K. Nielsch
Institute of Materials Science
Technische Universität Dresden
01062 Dresden, Germany
X. Ding
Key Laboratory of Advanced Display and System Application
Ministry of Education, Shanghai University
Shanghai 200072, China
M. Laitinen, J. Julin, M. Kivekäs, T. Sajavaara
Department of Physics
University of Jyvaskyla
Jyväskylä FI-40014, Finland

The ORCID identification number(s) for the author(s) of this article can be found under https://doi.org/10.1002/aelm.202101334.



**DOI: 10.1002/aelm.202101334**

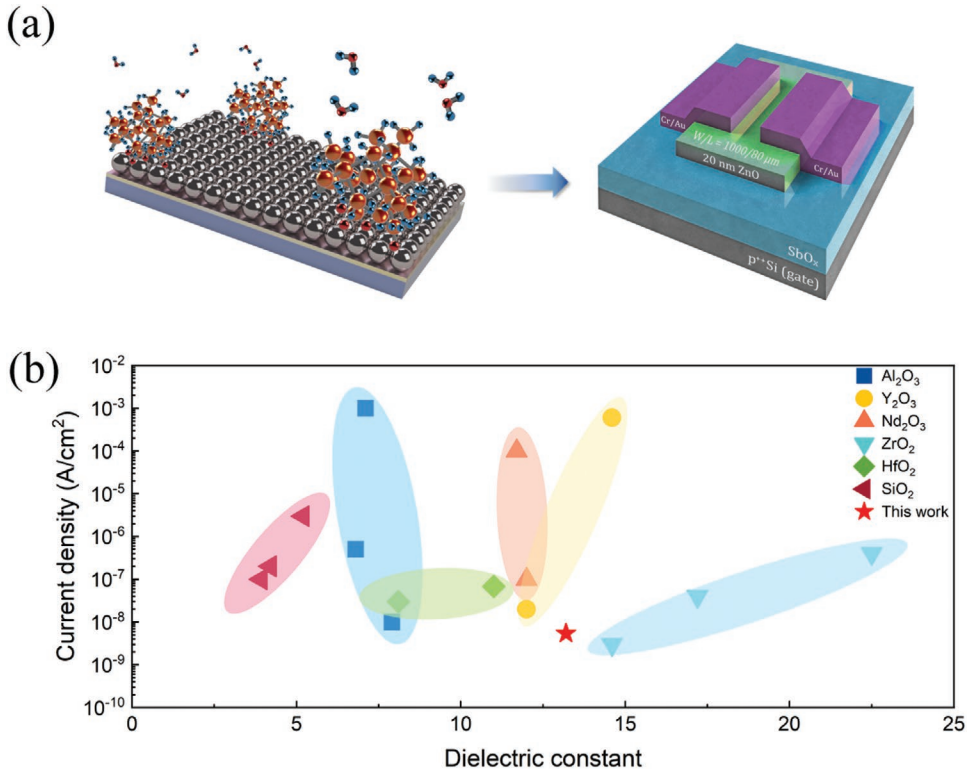


**Figure 1.** a) Schematic of the process from thin film to device. b) Summary of dielectric properties for high-*k* materials.[19,20]

dielectric property.[9] The breakdown field can reach a value of 2.5 MV $cm^{-1}$ for a dielectric layer thickness of 100 nm.[10] Liu et al. showed that monolayer molybdenum disulfide field-effect transistors supported by $Sb_2O_3$ dielectric substrate exhibit reduced transfer-curve hysteresis compared with when using $SiO_2$ substrate.[11] However, it should be mentioned that $Sb_2O_3$ is classified as a carcinogen in large quantities.

In addition to the composition of metal oxides, the thin film preparation method plays an important role in achieving high-performance devices. Thin films grown by magnetron sputtering and pulsed laser deposition techniques can lead to surface scattering and deterioration of the device stability.[12] Additionally, solution-based deposited (such as sol–gel and inkjet printing) thin films require very high postannealing temperatures to achieve a high-densification metal–oxygen–metal (M—O—M) structure. Furthermore, the reproducibility in these mentioned films is not always satisfactorily achievable.[13] The electrical properties of TFT devices are greatly influenced by the interface defects between the channel and insulator well as the roughness of the layers.[14] It is well-known that a dielectric material with a smooth surface is essential to enable proper electronic device function.[1] For instance, despite having a high dielectric constant, classical high-*k* thin films such as $ZrO_2$ and $HfO_2$ are susceptible to forming a crystal structure with a rough surface.[15] In addition, the dielectric property of high-*k* layer strongly depends on the preparation process, which dominates the impurity and residue groups in the material structure.[16] Therefore, it is crucial to look for an appropriate deposition technique with high reproducibility, excellent thickness controllability, accurate chemical composition control, and low growth temperatures.

The atomic layer deposition (ALD) technique offers the highest conformality among all deposition techniques as well as atomic layer control over wide deposition temperature ranges, thanks to sequential and self-limiting surface reactions.[17] Due to the high conformability of ALD process, it is widely used in the coating of metal oxide thin films. To the best of our knowledge, the dielectric properties of ALD-processed $SbO_x$ have never been explored before. Herein, we develop $SbO_x$ dielectric thin films by thermal ALD using $SbCl_5$ and $Sb(NMe_2)_3$ as antimony reactants and $H_2O$ and $H_2O_2$ as oxidizers at low temperatures (80–200 °C). The electrical and structural properties of deposited $SbO_x$ films were investigated systematically. The amorphous structure of $SbO_x$ deposited in this study presents a smooth surface, resulting in a high-quality dielectric/semiconductor interface. Furthermore, the dielectric constant of $SbO_x$ is higher than 13, resulting in a satisfactory capacitance. Additionally, the elemental concentration in the films was studied by time-of-flight elastic recoil detection analysis (ToF-ERDA) to correlate the level of impurities with the device performance.[18] Furthermore, the ALD ZnO semiconductor material, owing to its nontoxicity, low cost, and high mobility characteristics, was integrated into a $SbO_x$ dielectric and fabricated TFT device. In this study, the ALD process provides an excellent interface state between the channel and insulator, boosting the performance of TFT devices. Therefore, as a new high-*k* material, ALD-processed $SbO_x$ is a great candidate that merits further research and development.

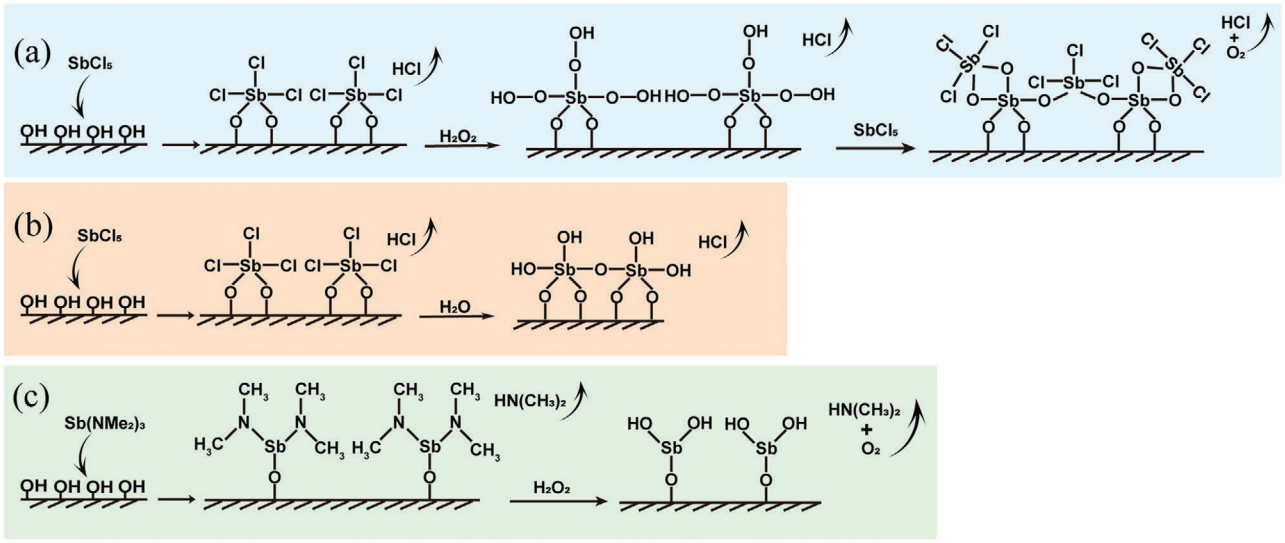


**Figure 2.** Schematic diagram of the reaction mechanism for ALD $SbO_x$ using different precursors: $SbCl_5$ and a) $H_2O_2$ or b) $H_2O$, c) $Sb(NMe_2)_3$ and $H_2O_2$.

## 2. Results and Discussion

To understand the growth behavior and effect of using different precursors on the quality and performance of the as-grown $SbO_x$ thin films, $H_2O$ and $H_2O_2$ oxidants were selected to react with $SbCl_5$ and $Sb(NMe_2)_3$. The postulated mechanism is shown in **Figure 2**. The hydroxyl saturated surface is exposed to the Sb precursor, which reacts with the hydroxyl group, leaving behind a −Cl (or $-CH_3$) terminated surface. The −Cl (or $-CH_3$) surface will be exposed to the oxygen source ($H_2O_2$ or $H_2O$) and react on the surface to leave one layer of a $SbO_x$ thin film. The carrier gas removes excess precursors and byproducts in each half ALD cycle.

Based on the reaction mechanism, the $SbO_x$ growth properties with respect to different precursors at different chamber temperatures are shown in **Figure 3**. The thickness and the X-ray reflectivity (XRR) patterns are shown in Figures S1 and S2 (Supporting Information), respectively. For all thin films, the growth per cycle (GPC) decreases as the deposition temperature ($T_D$) increases. This is probably due to the desorption of reactive surface sites, such as −OH, from the substrate at higher temperatures.[21] When sufficient Sb precursors are pulsed into the chamber and the surface reaction is not limited, the amount of −OH groups on the surface is the crucial condition for determining the growth rate during the ALD process. Thus, the density of −OH decreases with increasing $T_D$, leading to a reduction in the GPC.[22] It should be mentioned that the $SbO_x$ deposited using $SbCl_5$ and different oxygen sources shows a very different growth rate. For example, the GPC for $SbO_x$ ($SbCl_5$ + $H_2O$) is ≈1.3 Å, but it is only 0.9 Å for

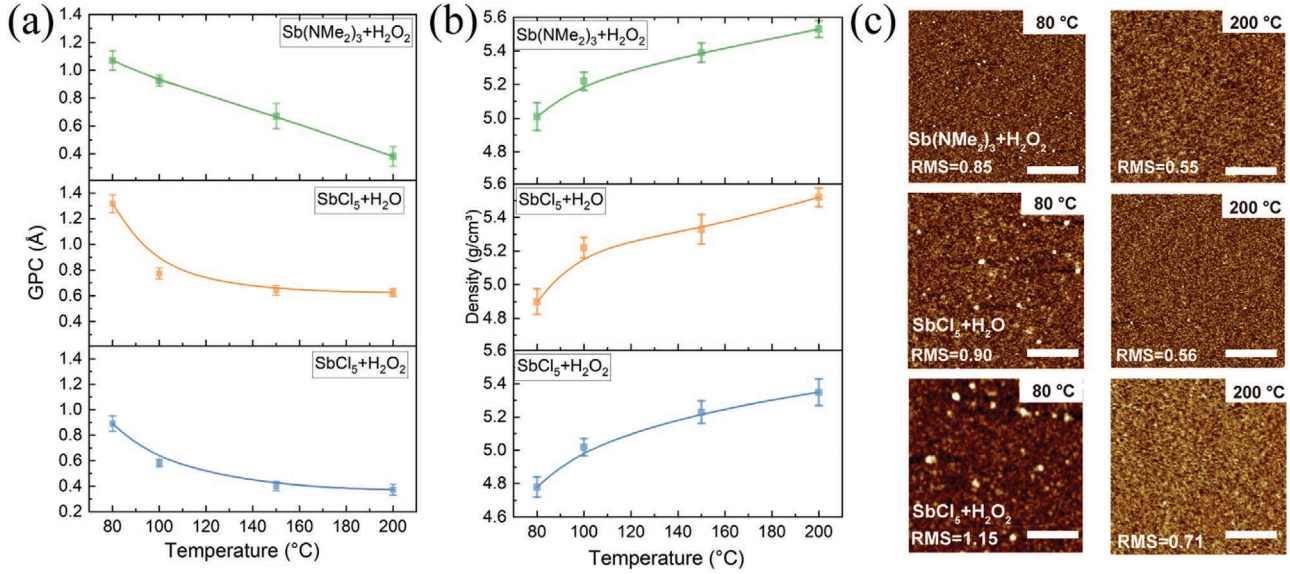


**Figure 3.** a) The growth rate, b) density, and c) AFM images (scale bar: 1 µm) of the $SbO_x$ thin films.

$SbO_x$ synthesized from the reaction between $SbCl_5$ and $H_2O_2$. According to the Langmuir adsorption isotherm, the number of surface hydroxyl groups strongly depends on the vapor pressure of the oxidant precursor.[23] The vapor pressure of $H_2O_2$ is 18.4 Torr, which is lower than that of $H_2O$ (23.8 Torr) at room temperature. The relatively lower density of −OH groups leads to a lower GPC for $SbO_x$ using $SbCl_5$ and $H_2O_2$.

The density values for the thin films obtained from the calculated fit to the XRR patterns are shown in Figure 3b. As the $T_D$ increases, the density of the $SbO_x$ thin films increases from ≈4.9 g cm$^{-3}$ at 80 °C to ≈5.5 g cm$^{-3}$ at 200 °C. Impurity incorporation induced by a higher growth rate, as well as partial detachment of chemical legends during the purging process due to a lower deposition temperature, may affect thin film density in this case. The surface morphologies of $SbO_x$ were studied by atomic force microscopy (AFM) analyses with scanned areas of 5 × 5 μm$^2$, as shown in Figure 3c and Figure S3 (Supporting Information). The root mean squared value of the surface for $SbO_x$ films grown using $SbCl_5$ is slightly higher than that of $Sb(NMe_2)_3$. The differences in the obtained roughness values can be attributed to several facts, i.e., i) films grown using metal chloride precursors always have an "incubation" time, imposing few ALD cycles to fulfill the requirement for uniform coverage of a hydrogen-terminated Si surface, which can lead to difficulty for the deposition at the initiating cycles and to a high degree of surface roughness,[24] ii) the formation of HCl as a byproduct that etches the thin films, leading to a nonuniform and rough surface.[25]

The scanning electron microscopy (SEM) images are shown in Figures S4 and S5 (Supporting Information). There is a clear interface between the deposited thin films and Si substrate. As mentioned before, inhomogeneous $SbO_x$ deposition is observed when $Sb(NMe_2)_3$ and $H_2O$ are used as precursors, probably resulting from the weak oxidizing ability of $H_2O$ (Figure S5e, Supporting Information). Deposition of 900 cycles of $SbO_x$ using $Sb(NMe_2)_3$ and $H_2O_2$ results in a thickness of ≈106.2 nm at a $T_D$ of 80 °C, while it is reduced to ≈36.6 nm when the $T_D$ is increased to 200 °C, which is consistent with the XRR results. The transmission electron microscopy (TEM) analyses (Figure S5c, Supporting Information) and grazing incidence X-ray diffraction patterns (Figure S5d, Supporting Information) confirm the amorphous nature of all $SbO_x$ thin films deposited using different precursors at the studied deposition temperatures.

The X-ray photoelectron spectroscopy (XPS) was used to identify the binding energies and chemical states of the elements in the $SbO_x$ thin films presented in **Figure 4**a–d and Figure S6 (Supporting Information). The C 1s state was used as a reference to calibrate the binding energy. The normalized O 1s area is shown in Figure 4b. The thin film deposited at 200 °C shows a smaller O 1s area compared to other films, which is consistent with the analysis of the change in the coordination number for Sb. Interestingly, the XPS peaks were found to shift toward lower binding energies for increasing $T_D$. This phenomenon can be explained by two mechanisms: i) the progressive oxidization of Sb from SbOCl [or $Sb(NMe_2)_2OH$] to $SbO_x$,[26] and ii) the decrease in the coordination number of Sb (from $Sb_2O_5$ to $Sb_2O_3$) can result in lower binding energy.[27] Although the O 1s spectra overlap with the Sb 3d spectra, the use of some strict rules makes it possible to separate out the O 1s spectra;[28] i) the full width at half maximum of $3d_{3/2}$ is equal to that of $3d_{5/2}$, ii) the center distance between $3d_{5/2}$ and $3d_{3/2}$ is 9.34 eV, and iii) the area of $3d_{5/2}$ is theoretically 1.5 times

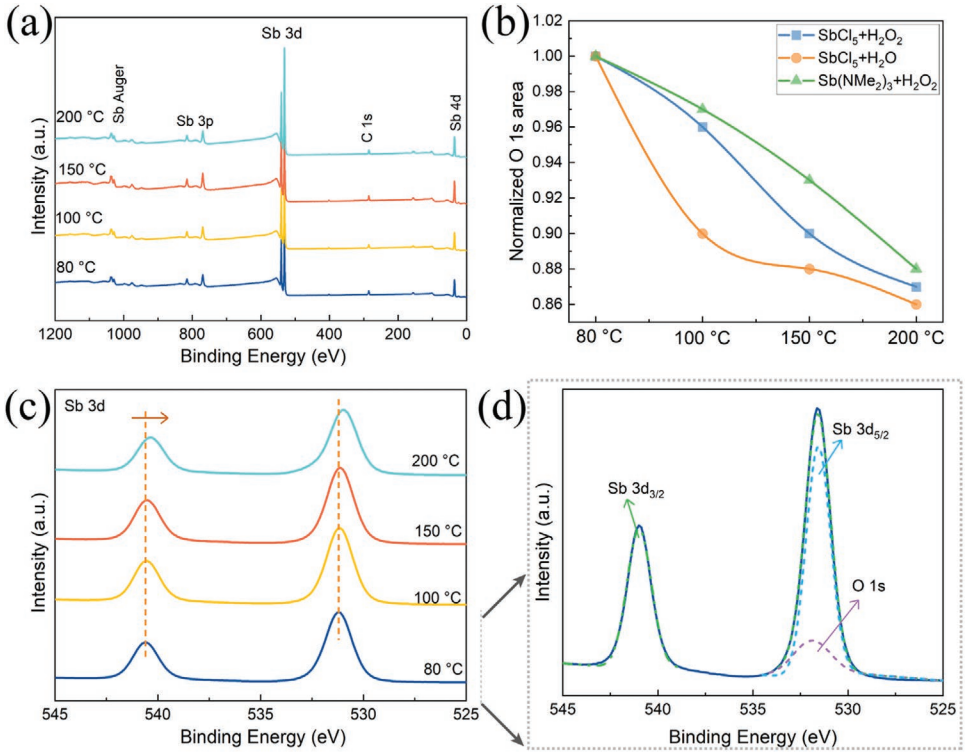


**Figure 4.** a) XPS survey for Sb 3d for $SbO_x$ thin films ($Sb(NMe_2)_3$ and $H_2O_2$). b) Normalized O 1s area. c) Sb 3d spectra and d) fitting result.

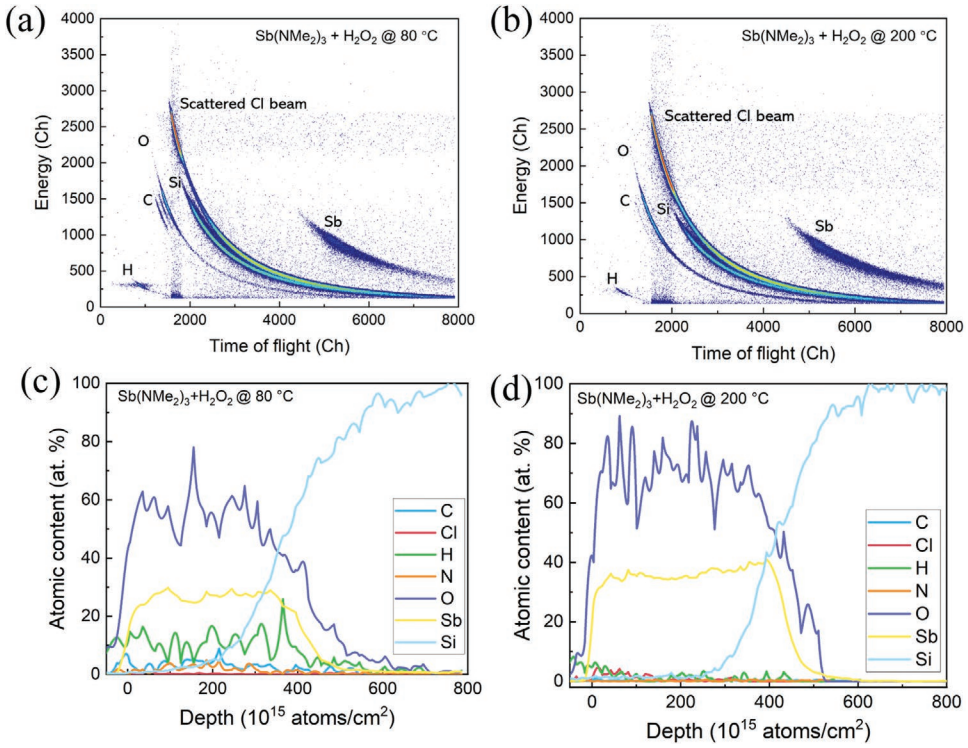


**Figure 5.** ERDA spectrum of ALD $SbO_x$ deposited using $Sb(NMe_2)_3$ and $H_2O_2$ at a) 80 °C and b) 200 °C. In the 2D histogram of raw spectra, light elements are observed more toward the bottom left corner of the plot, where the energy and time of flight are at their minimum. A lower energy and a longer time-of-flight for each element indicate that the events originate deeper from the sample. c,d) ERDA depth profile of $SbO_x$ on a Si substrate, extracted by analyzing the spectra shown using the Potku software package.

larger than that of $3d_{3/2}$. It is known that a strong M—Cl (M is the metal atom) bond can hardly be replaced by a M—O bond during ALD. The first principle calculation shows that a high $T_D$ is necessary to overcome this high activation energy barrier.[29] In addition, a high $T_D$ can effectively reduce the incorporation of Cl impurities into the synthesized film[25] (see Figure S7 in the Supporting Information).

ToF-ERDA analysis was used to detect different elements, such as Sb, O, H, C, and Cl, in the $SbO_x$ thin films, as presented in **Figure 5**a–d and **Table 1**. The content of some impurities, such as H, can strongly affect the performance of TFT devices.[20] Although an overabundance of hydrogen in the dielectric layer of TFTs is assumed to deteriorate device performance due to the generation of excess carriers, a controlled amount of hydrogen can efficiently passivate the electrode/$SbO_x$ interfacial states under a certain electric field and form an electric double layer, leading to a high areal capacitance.[30] Therefore, precise analysis of the H content is crucial for ALD films grown using hydrogen-containing precursors. ToF-ERDA outperforms X-ray photoelectron spectroscopy in terms of sensitivity and depth resolution, and it outperforms time-of-flight secondary ion mass spectrometry in terms of quantitative evaluation capabilities, which is suitable for detecting smaller trace of H, Cl, and C, and the Sb:O ratio in the $SbO_x$ film. From the ERDA measurement, it can be concluded that the Sb/O ratio increases with increasing deposition temperature. The same behavior was observed for hydrogen content for increasing deposition temperature, i.e., reduction of hydrogen content from ≈11.2% to ≈0.6% upon increase of the deposition temperature of $SbO_x$ using $Sb(NMe_2)_3$ and $H_2O_2$ from 80 to 200 °C. It should also be mentioned that the materials deposited at lower temperatures (80 °C) were not stable and were partially

**Table 1.** Elemental compositions of ALD-grown films determined by ToF-ERDA.

| Sample | $T_D$ [°C] | *H* [at%] | *C* [at%] | Cl [at%] | N [at%] | Sb [at%] | Sb:O |
|---|---|---|---|---|---|---|---|
| $SbCl_5 + H_2O_2$ | 80 | 22 ± 2 | 0.3 ± 0.06 | 1 ± 0.3 | – | 25 ± 2 | 0.52 |
| | 200 | 3.2 ± 1.5 | 0.3 ± 0.15 | 0.8 ± 0.3 | – | 34.5 ± 1.5 | 0.56 |
| $SbCl_5 + H_2O$ | 80 | 19 ± 2 | 0.6 ± 0.2 | 1.5 ± 0.5 | – | 25 ± 2 | 0.48 |
| | 200 | 5.5 ± 1.5 | 0.1 ± 0.08 | 0.9 ± 0.3 | – | 31 ± 3 | 0.51 |
| $Sb(NMe_2)_3 + H_2O_2$ | 80 | 11.2 ± 2 | 4.0 ± 1.0 | – | 2.4 ± 0.8 | 26.5 ± 1.5 | 0.47 |
| | 200 | 0.6 ± 0.3 | 0.22 ± 0.07 | – | 0.13 ± 0.06 | 33 ± 2 | 0.53 |

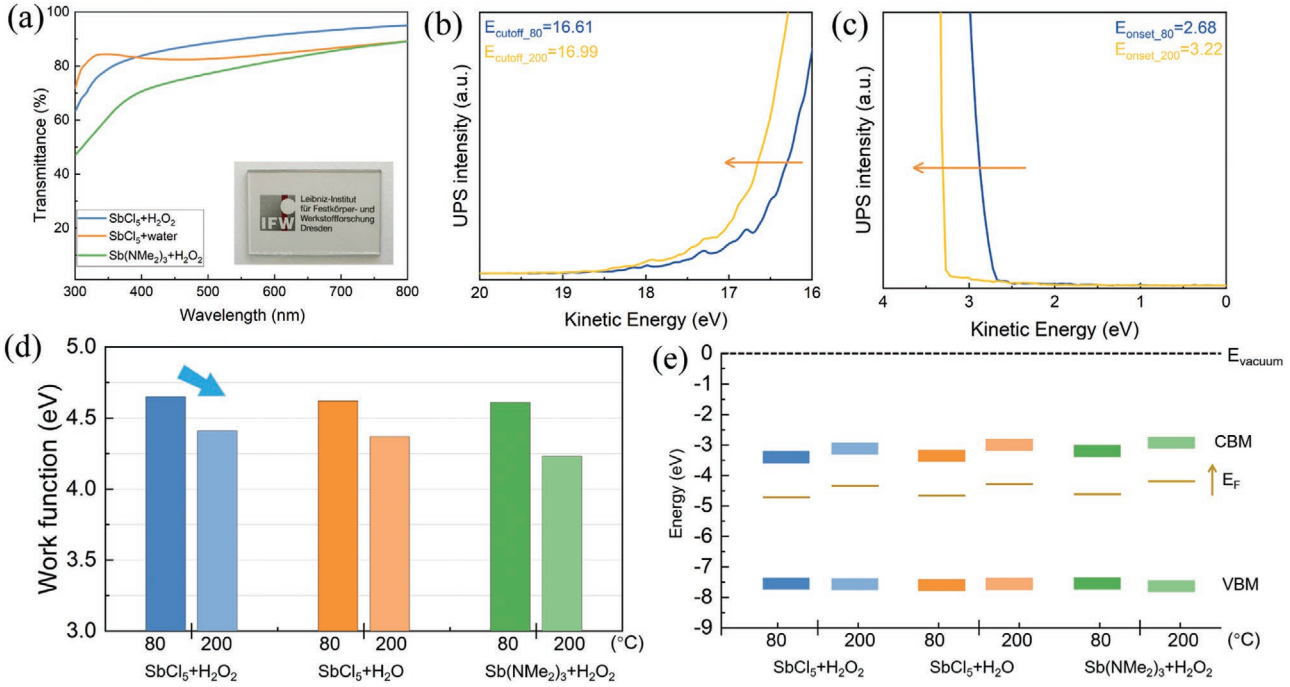


**Figure 6.** a) Transmittance for $SbO_x$ grown at 200 °C. UPS spectra obtained for b) the secondary electron onset and c) valence band edge for a $SbO_x$ thin film grown using $Sb(NMe_2)_3$ and $H_2O_2$. d) The work function and e) the band structure diagram for all $SbO_x$ thin films.

destroyed by the ion beam during the measurement, which may generate some ambiguity in the ERDA analysis results for such samples. A more detailed picture of the elemental composition for all deposited films is presented in Table 1.

To evaluate the optical properties of the deposited $SbO_x$ films, films were grown onto a quartz glass substrate, as shown in **Figure 6**a and Figure S8 (Supporting Information). In the visible range, the thin films are highly transparent at 80%, which can also be proven by the optical image shown in the inset figure, favoring potential application in transparent electronic devices. The obtained bandgap values are different for $SbO_x$ deposited using different precursors. It is noted that the bandgap values increase as the $T_D$ is increased (Figure S8, Supporting Information). Soon and co-workers calculated the band structure of $SbO_x$ by density functional theory.[31] They found that with the transition of $SbO_x$ phase from $Sb_2O_5$ to $Sb_2O_3$, the bandgap increases obviously. In our work, $SbO_x$ is a mixture of $Sb_2O_5$ (low bandgap) and $Sb_2O_3$ (high bandgap). The Sb:O ratio calculated by ToF-ERDA (Table 1) and XPS (Figure 4b) shows that the majority of the phase is $Sb_2O_3$ with a relative higher bandgap. By increasing the deposition temperature and reducing of coordination number of Sb, we will have more $Sb_2O_3$ and as a result, higher bandgap.

The combination of ultraviolet photoelectron spectroscopy (UPS) and XPS provides knowledge for the electronic structure and energy band positions of various materials. UPS spectra were obtained to explore the band structure of the $SbO_x$ thin films. A clear shift of the secondary electron cutoff ($E_{cutoff}$) and the valence band edge to higher energies by increasing the deposition temperature can be observed in all three systems, as shown in Figure 6b,c and Figure S9 (Supporting Information). From the secondary cutoff at high binding energy, the work function ($\varphi$) was determined by subtracting the cutoff energy from the photon energy (21.2 eV) and is presented in Figure 6d. The results confirm the reduction of $\varphi$ due to increased deposition temperature and relocation of the Fermi level toward the conduction band edge. Kumar and co-workers reported the same phenomenon in their study of $Ba_{0.5}Sr_{0.5}TiO_3$ system.[32] The induced vacancies disrupt the orbital character and cause Fermi level shift toward conduction band. Another explanation is that amorphous $Sb_2O_3$ behaves more as an n-type material than $Sb_2O_5$.[33] As mentioned before, the thin films underwent a phase transition from $Sb_2O_5$ to $Sb_2O_3$ when the deposition temperature was raised, as shown in ToF-ERDA (Table 1) and XPS (Figure 4b) results. Therefore, the presence of more $Sb_2O_3$ phase in the thin film at high temperatures might lead the Fermi level to be closer to the conduction band. The corresponding valence band maximum was calculated, and the energy band diagram is presented in Figure 6e. Previous reports indicate that an offset for $\varphi$ can result from the use of different processing conditions and composition variation.[34] Here, we postulate that the decrease in the coordination number of Sb (from $Sb_2O_5$ to $Sb_2O_3$) at higher temperature can reduce $\varphi$.

Metal–insulator–metal structured capacitors were fabricated to evaluate the electrical and dielectric properties of ALD $SbO_x$ thin films deposited using different precursors and deposition temperatures. **Figure 7**a and Figure S10 (Supporting Information) show the leakage current behavior of the $SbO_x$ dielectrics. A significant leakage current density is observed for all $SbO_x$ thin films deposited at 80 °C (Figure S10, Supporting Information). At lower deposition temperatures, the thin films contain a high content of impurities originating from incomplete decomposition of precursors (see Table 1), which act as leakage

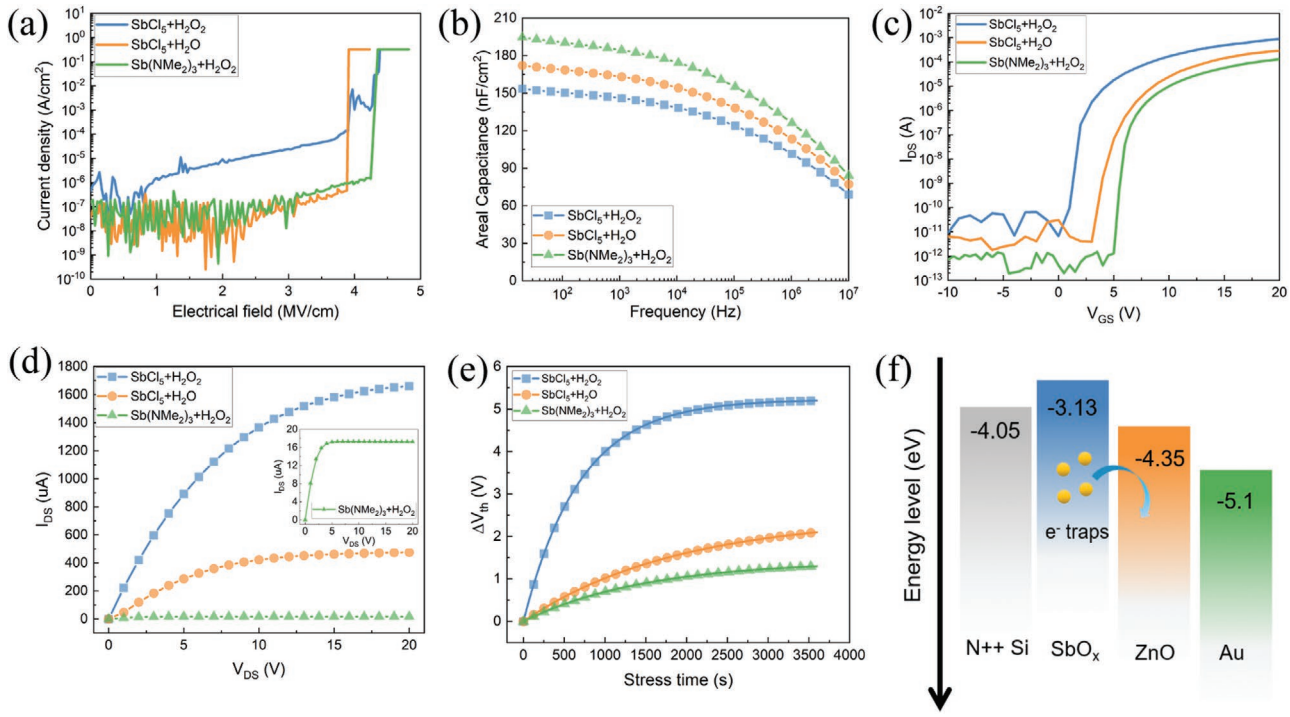


**Figure 7.** a) Leakage current density characteristics and b) capacitance frequencies for $SbO_x$ dielectrics deposited at 200 °C. c) Transfer curves for ZnO/$SbO_x$ thin film transistors. d) Output curve with a fixed gate voltage of 20 V. e) Positive bias stress test results. f) Illustration of the metal–insulator–semiconductor mechanism for electron emission.

current paths and lead to a high current density. At higher deposition temperatures, a decreased leakage current can be an indication of full decomposition of precursors, and, as a result, less impurities in the final deposited film, which agrees with the density values obtained using XRR analyses and the impurity content indicated by the ToF-ERDA method. Furthermore, at a deposition temperature of 200 °C, a lower current density and higher breakdown field are measured for films grown using $Sb(NMe_2)_3$ compared to that for films grown using $SbCl_5$ (Figure 7a), which indicates a higher density of traps in the metal–oxide framework of films derived from chlorine-based precursors. Kukli et al. observed that the trap density in films grown from chlorine-based precursors is higher than that for films grown from different precursors,[35] resulting in a higher current density and lower breakdown field. Figure 7b shows the capacitance–frequency properties of the $SbO_x$ dielectric grown at 200 °C with different precursors. The $SbO_x$ thin film deposited by $Sb(NMe_2)_3$ shows a high dielectric constant of about 13.2 (Figure S10d, Supporting Information).

To achieve low-leakage current TFTs, the offset of the dielectric conduction band minimum should be at least 1 eV relative to the semiconductor material in an n-type transistor.[36] A band offset of higher than 1 eV effectively confines the charges within the ZnO channel during the device measurement (Figure S11, Supporting Information). To confirm the possible application of $SbO_x$ thin films as a dielectric layer in TFTs, bottom-gated TFTs integrated with an ALD ZnO channel layer were fabricated. The typical transfer curves are shown in Figure 7c. The key electrical parameters are summarized in **Table 2**. Here, a high field-effect mobility of 12.4 $cm^2\ V^{-1}\ s^{-1}$ and a minimum subthreshold swing (SS) value of 0.22 V $dec^{-1}$ for TFTs based on the $Sb(NMe_2)_3$ precursor were calculated via the derivative of the transfer curve determining the slope. However, the TFT based on the $SbO_x$ dielectric grown from $SbCl_5$ shows a relatively unsatisfactory performance, i.e., a low mobility of 6.3 $cm^2\ V^{-1}\ s^{-1}$ and a high SS value of 0.88 V $dec^{-1}$. Moreover, the maximum areal density of states ($N_{trap}$) was further obtained from SS values using the following formula[37]

$$SS = \frac{k_B T \ln 10}{q}\left[1 + \frac{q^2}{C_{ox}} N_{trap}\right] \quad (1)$$

**Table 2.** Performance parameters for ZnO/$SbO_x$ TFTs with ZnO as the channel and $SbO_x$ as the dielectric layer ($\mu$, $V_{th}$, $I_{on}/I_{off}$, SS, and $N_{trap}$ are the field-effect mobility, threshold voltage, ratio of on and off currents, subthreshold swing, and trapping state).

| Precursors | $V_{th}$ [V] | $\mu$ [$cm^2\ V^{-1}\ s^{-1}$] | $I_{on}/I_{off}$ | SS [V $dec^{-1}$] | $N_{trap}$ [$eV^{-1}\ cm^{-2}$] |
|---|---|---|---|---|---|
| $SbCl_5$ and $H_2O_2$ | 2.57 | 6.3 | $5 \times 10^7$ | 0.88 | $7.5 \times 10^{12}$ |
| $SbCl_5$ and $H_2O$ | 4.72 | 8.7 | $2 \times 10^7$ | 0.65 | $3.7 \times 10^{12}$ |
| $Sb(NMe_2)_3$ and $H_2O_2$ | 5.03 | 12.4 | $4 \times 10^8$ | 0.22 | $1.1 \times 10^{12}$ |

where $k_B$ is the Boltzmann's constant, $T$ is the temperature in Kelvin, $C_{ox}$ is the gate oxide capacitance, and $q$ is the electron charge. As shown in Table 2, a low $N_{trap}$ was obtained for $SbO_x$ grown from $Sb(NMe_2)_3$- and $H_2O_2$-based TFTs, indicating an excellent interface between the channel layer (ZnO) and dielectric layer ($SbO_x$).[20] Figure 7d shows the output characteristics of TFTs, clearly indicating pinch-off behavior and drain current saturation at high $V_{DS}$.

The electrical stability is also carried out under long-term positive bias stress (PBS), i.e., applying constant positive bias stress (+20 V) between the drain and source for 1 h followed by measurement of the transfer curve (Figure S12, Supporting Information). When a positive voltage is applied under atmospheric conditions, electrons will accumulate in the ZnO semiconductor. The surrounding oxygen molecules with large electronegativity can capture electrons from the conduction band to form $O^{2-}$ species. Therefore, the carriers in the ZnO layer can be removed, leading to a shift in the positive threshold voltage ($\Delta V_{th}$).[20] The energy band diagram for TFTs under PBS conditions and the variations in the threshold voltage shift ($\Delta V_{th}$) as a function of stress time are shown in Figure 7e and Figure S13 (Supporting Information). It can be observed that the TFT based on $SbCl_5$ and $H_2O_2$ shows a higher voltage shift of 5.1 V, while for the TFT-based $Sb(NMe_2)_3$, the voltage shift is only 1.2 V, which reveals that there are only a small number of defects at the interface between the semiconductor and dielectric layer.

The superior performance of TFTs based on the $Sb(NMe_2)_3$ precursor can be explained from different aspects. First, chlorine is a strongly electronegative impurity and strongly degrades the dielectric property of $SbO_x$ thin films. However, the $SbO_x$ thin film grown from the $Sb(NMe_2)_3$ precursor possesses a low content of impurities, revealing a lower density of states. Second, the amorphous structure presents smoother surfaces than the crystalline surfaces, resulting in a good quality dielectric/semiconductor interface. In addition, the smooth interface can decrease the surface scattering and is beneficial to the performance of TFT devices.[38] Third, it is postulated that low-temperature-processed $SbO_x$ dielectrics generate intrinsic donor-like electron traps. For increasing transverse $V_{GS}$, the traps inject electrons into the ZnO semiconductor by thermally activated emission, increasing the electron concentration in bulk ZnO and resulting in a high field-effect mobility in TFT devices (Figure 7f).[8,39] Furthermore, the right amount of hydrogen can efficiently passivate the interfacial states and enhance the TFT device performance.[20] Finally, in oxide semiconductors (ZnO), electrical conduction is mainly dominated by electron-trapping sites (**Figure 8**a). Based on the multiple-trapping-and-release model, trapping sites can be introduced by electron transport. Most of the electrons fill the localized state before participating in conduction transport (Figure 8b), and only a small amount of electrons can move into the transport bands. The $SbO_x$ dielectric provides a high capacitance, which exhibits a stronger electric field and provides more energy to electrons. Therefore, a large number of electrons easily fill the lower-lying localized state and are rapidly trapped in the upper-lying localized states, which can remarkably enhance the TFT mobility.[20,40]

## 3. Conclusion

In summary, $SbO_x$ thin films were successfully synthesized using a new combination of antimony reactants and oxidizers, namely, $SbCl_5$, $Sb(NMe_2)_3$, $H_2O$, and $H_2O_2$, in the temperature range of 80–200 °C. Furthermore, the dielectric properties of ALD-processed $SbO_x$ thin films were fully studied. Thin film structural and compositional characterization using XRD, TEM, AFM, and XRR confirms the uniformity, high density, and amorphous nature of all the films studied. Additionally, increasing the deposition temperature results in the deposition of denser and purer $SbO_x$ phases, as proved by ToF-ERDA and XPS. The UPS spectra confirm that the work function decreases and the Fermi level shifts toward the conduction band edge with increasing deposition temperature. The TFT performance of devices is affected by the type of precursor and deposition temperature. For $SbCl_5$-based $SbO_x$, it is easy to form Sb—O bonds during the ALD process at high deposition temperatures due to the high bonding energy of M—Cl. The Cl impurity can degrade the dielectric performance of $SbO_x$ thin films and result in a high leakage current and a low breakdown electric field. In comparison, the $Sb(NMe_2)_3$-based $SbO_x$ films demonstrate good dielectric properties, i.e., a breakdown field of ≈4 MV $cm^{-1}$ and a high areal capacitance of ≈200 nF $cm^{-2}$ at 200 °C. To evaluate the performance of deposited films in

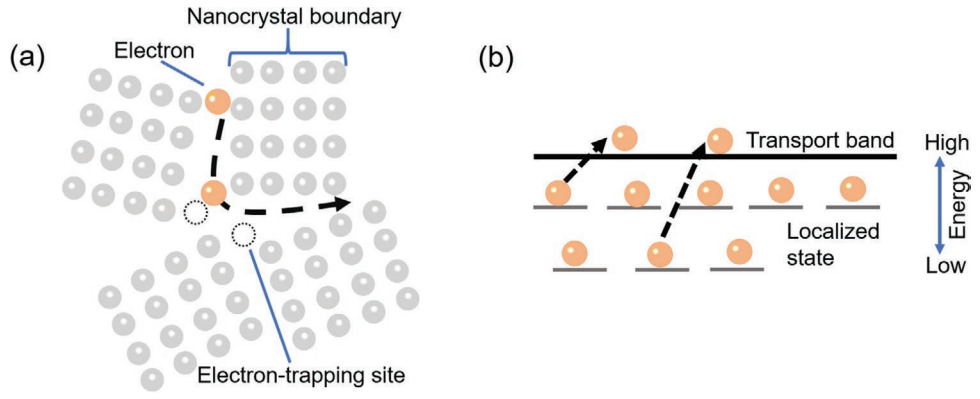


**Figure 8.** a) Schematic of the electron-transporting mode. b) Energy band diagram of oxide semiconductor thin films. A very high electric field is induced by $SbO_x$, which makes it easier to quickly trap electrons in the upper-lying localized states.

TFT devices, ZnO/$SbO_x$ thin film transistors were fabricated. A TFT with a $SbO_x$ dielectric layer deposited using $Sb(NMe_2)_3$ and $H_2O_2$ at 200 °C showed the best performance, such as a high $\mu$ of 12.4 $cm^2\ V^{-1}\ s^{-1}$, an $I_{on}/I_{off}$ ratio of $4 \times 10^8$, a sharp SS of 0.22 V $dec^{-1}$, and a low $N_{trap}$ of $1.1 \times 10^{12}\ eV^{-1}\ cm^{-2}$. After applying a voltage stress of 10 V for a period of 3600 s, the $\Delta V_{th}$ for the $SbO_x$–ZnO TFT is only 1.2 V. The findings here will benefit the development of new microelectronics and further applications.

## 4. Experimental Section

*Deposition of $SbO_x$ Thin Film*: $SbO_x$ thin films were deposited onto Si and quartz glass substrates using a thermal ALD reactor (Veeco Savannah S200) at different deposition temperatures of 80, 100, 150, and 200 °C. $SbCl_5$ and $Sb(NMe_2)_3$ were used as antimony reactants, and $H_2O$ and $H_2O_2$ were used as oxidizers. $SbCl_5$ and $Sb(NMe_2)_3$ were maintained at 40 °C and room temperature, respectively, and were pulsed into the reaction chamber with a continuous $N_2$ flow as the carrier gas. The optimized pulse and purge times for one ALD deposition cycle (Sb precursor/$N_2$/$H_2O$ or $H_2O_2$/$N_2$) were 0.15/10/0.5/10 s. No reaction was observed using $Sb(NMe_2)_3$ and $H_2O$, while both water and $H_2O_2$ could oxidize $SbCl_5$ during the ALD process.

*Device Fabrication*: 16 nm ZnO was deposited onto 60 nm thick $SbO_x$ thin films. Cr/Au electrodes were deposited as the source/drain of TFT devices by magnetron sputtering with a channel width ($W$) of 1000 µm and channel length ($L$) of 80 µm. In order to evaluate the dielectric properties of $SbO_x$, a metal–insulator–metal (MIM) structure was fabricated. $SbO_x$ thin film was deposited on the highly doped Si substrate (0.001 Ω cm). Then, the Cr/Au was deposited as an upper electrode by sputtering using a shadow mask with a diameter of 1 mm. The schematic of MIM is shown in Figure S10 (Supporting Information).

*Thin Film and Device Characterization*: The thickness of the thin films was measured using XRR (Philips X'Pert Pro MRD). The surface morphology was studied by AFM (Bruker Dimension Icon) and field-emission scanning electron microscopy (Sigma 300-ZEISS FESEM). XPS was conducted using a Thermo Scientific K-Alpha+. UPS was performed using an ESCALAB 250Xi (Thermo) system. The samples were excited with the resonance line He-I ($h\nu$ = 21.2 eV). All measurements were carried out under the same bias voltage of –10 V. The elemental composition and depth profiles for thin films were obtained by ToF-ERDA with a 6.8 MeV $^{35}Cl^{3+}$ beam. The scattering angle was 15° or 20° using a mirror measuring geometry. ToF-ERD data were analyzed using Potku software.[41] The optical transmission was measured using a double-beam spectrophotometer (U-3900). The field-effect mobility ($\mu$) and SS were calculated using the following equations

$$I_D = \left(\frac{W}{2L} C_i \mu\right)(V_{GS} - V_{th})^2 \tag{2}$$

$$SS = \frac{dV_{GS}}{d(\log I_D)} \tag{3}$$

where $W$ and $L$ are the channel width and length, respectively, $C_i$ is the areal capacitance of the dielectric, $V_{th}$ is the threshold voltage, and $V_{GS}$ is the gate voltage. The bandgap of the thin films was extracted by using the Tauc model

$$(\alpha \cdot h\nu)^2 = A(h\nu - E_g) \tag{4}$$

where $\alpha$ is the absorption coefficient and $A$ and $h\nu$ are a constant and the photon energy, respectively.

## Supporting Information

Supporting Information is available from the Wiley Online Library or from the author.

## Acknowledgements

This work was supported by the Program of Collaborative Research Centers in Germany (Grant No. SFB 1415). The research leading to this result was supported by the RADIATE project under the Grant Agreement No. 824096 from the EU Research and Innovation program HORIZON 2020. A.B. also acknowledges the Alexander von Humboldt-Stiftung for Postdoctoral Research Fellow funding. Special thanks to Dr. Heiko Reith for technical assistance and Ronald Uhlemann for preparation of the illustrations.

Open access funding enabled and organized by Projekt DEAL.

## Conflict of Interest

The authors declare no conflict of interest.

## Data Availability Statement

Research data are not shared.

## Keywords

atomic layer deposition, high-$k$ dielectric, low temperature, oxide semiconductor, ToF-ERDA

Received: December 7, 2021
Revised: February 1, 2022
Published online:

[1] B. Wang, W. Huang, L. Chi, M. Al-Hashimi, T. J. Marks, A. Facchetti, *Chem. Rev.* **2018**, *118*, 5690.
[2] a) K. Lu, J. Zhang, D. Guo, J. Xiang, Z. Lin, X. Zhang, T. Wang, H. Ning, R. Yao, J. Peng, *IEEE Electron Device Lett.* **2020**, *41*, 417; b) J. W. Park, B. H. Kang, H. J. Kim, *Adv. Funct. Mater.* **2020**, *30*, 1904632; c) A. Liu, H. Zhu, H. Sun, Y. Xu, Y.-Y. Noh, *Adv. Mater.* **2018**, *30*, 1706364.
[3] E. Yarali, C. Koutsiaki, H. Faber, K. Tetzner, E. Yengel, P. Patsalas, N. Kalfagiannis, D. C. Koutsogeorgis, T. D. Anthopoulos, *Adv. Funct. Mater.* **2019**, *30*, 1906022.
[4] K. Nomura, H. Ohta, A. Takagi, T. Kamiya, M. Hirano, H. Hosono, *Nature* **2004**, *432*, 488.
[5] A. T. Oluwabi, A. Katerski, E. Carlos, R. Branquinho, A. Mere, M. Krunks, E. Fortunato, L. Pereira, I. O. Acik, *J. Mater. Chem. C* **2020**, *8*, 3730.
[6] N. P. Maity, R. Maity, S. Baishya, *High-k Gate Dielectric Materials: Applications with Advanced Metal Oxide Semiconductor Field Effect Transistors (MOSFETs)*, CRC Press, Boca Raton, FL **2020**.
[7] M. T. Bohr, R. S. Chau, T. Ghani, K. Mistry, *IEEE Spectrum* **2007**, *44*, 29.
[8] A. Zeumault, V. Subramanian, *Adv. Funct. Mater.* **2016**, *26*, 955.
[9] W. Han, P. Huang, L. Li, F. Wang, P. Luo, K. Liu, X. Zhou, H. Li, X. Zhang, Y. Cui, T. Zhai, *Nat. Commun.* **2019**, *10*, 4728.
[10] J. Peng, W. Pu, S. Lu, X. Yang, C. Wu, N. Wu, Z. Sun, H. T. Wang, *Nano Lett.* **2021**, *21*, 203.
[11] K. Liu, B. Jin, W. Han, X. Chen, P. Gong, L. Huang, Y. Zhao, L. Li, S. Yang, X. Hu, J. Duan, L. Liu, F. Wang, F. Zhuge, T. Zhai, *Nat. Electron.* **2021**, *4*, 906.

[12] X. Ding, J. Yang, C. Qin, X. Yang, T. Ding, J. Zhang, *IEEE Trans. Electron Devices* **2018**, *65*, 3283.
[13] A. Liu, H. Zhu, Y.-Y. Noh, *Mater. Sci. Eng., R* **2019**, *135*, 85.
[14] L. Qiang, X. Liang, Y. Pei, R. Yao, G. Wang, *Thin Solid Films* **2018**, *649*, 51.
[15] a) J. Yang, X. Yang, Y. Zhang, B. Che, X. Ding, J. Zhang, *Mol. Cryst. Liq. Cryst.* **2019**, *676*, 65; b) J. Zhang, X. Ding, J. Li, H. Zhang, X. Jiang, Z. Zhang, *Ceram. Int.* **2016**, *42*, 8115; c) D. M. Hausmann, R. G. Gordon, *J. Cryst. Growth* **2003**, *249*, 251.
[16] S. Kinnunen, K. Arstila, T. Sajavaara, *Appl. Surf. Sci.* **2021**, *546*, 148909.
[17] a) J. Sheng, J.-H. Lee, W.-H. Choi, T. Hong, M. Kim, J.-S. Park, *J. Vac. Sci. Technol., A* **2018**, *36*, 060801; b) R. B. Yang, J. Bachmann, M. Reiche, J. W. Gerlach, U. Gösele, K. Nielsch, *Chem. Mater.* **2009**, *21*, 2586; c) S. He, A. Bahrami, X. Zhang, I. G. Martínez, S. Lehmann, K. Nielsch, *Adv. Mater. Technol.* **2021**, 2100953; d) J. Yang, Y. Zhang, C. Qin, X. Ding, J. Zhang, *IEEE Trans. Electron Devices* **2019**, *66*, 1760.
[18] M. Laitinen, M. Rossi, J. Julin, T. Sajavaara, *Nucl. Instrum. Methods Phys. Res., Sect. B* **2014**, *337*, 55.
[19] a) L. Y. Liang, H. T. Cao, Q. Liu, K. M. Jiang, Z. M. Liu, F. Zhuge, F. L. Deng, *ACS Appl. Mater. Interfaces* **2014**, *6*, 2255; b) F. M. Li, B. C. Bayer, S. Hofmann, J. D. Dutson, S. J. Wakeham, M. J. Thwaites, W. I. Milne, A. J. Flewitt, *Appl. Phys. Lett.* **2011**, *98*, 252903; c) X.-H. Zhang, S. P. Tiwari, S.-J. Kim, B. Kippelen, *Appl. Phys. Lett.* **2009**, *95*, 312; d) R. Sarma, D. Saikia, P. Saikia, P. Saikia, B. Baishya, *Braz. J. Phys.* **2010**, *40*, 357; e) G. Geng, G. Liu, F. Shan, A. Liu, Q. Zhang, W. Lee, B. Shin, H. Wu, *Curr. Appl. Phys.* **2014**, *14*, S2; f) Y. Zhou, N. Kojima, K. Sasaki, *J. Phys. D: Appl. Phys.* **2008**, *41*, 175414; g) K. Kukli, K. Forsgren, M. Ritala, M. Leskelä, J. Aarik, A. Haårsta, *J. Electrochem. Soc.* **2001**, *148*, F227; h) J. Zhang, S. Liu, L. Kong, J. P. Nshimiyimana, X. Hu, X. Chi, P. Wu, J. Liu, W. Chu, L. Sun, *Adv. Electron. Mater.* **2018**, *4*, 1700628; i) L. Nyns, J. G. Lisoni, G. Van den Bosch, S. Van Elshocht, J. Van Houdt, *Phys. Status Solidi A* **2014**, *211*, 409; j) A. Kosola, J. Päiväsaari, M. Putkonen, L. Niinistö, *Thin Solid Films* **2005**, *479*, 152.
[20] J. Yang, Y. Zhang, Q. Wu, C. Dussarrat, J. Qi, W. Zhu, X. Ding, J. Zhang, *IEEE Trans. Electron Devices* **2019**, *66*, 3382.
[21] W. J. Lee, S. Bera, Z. Wan, W. Dai, J. S. Bae, T. E. Hong, K. H. Kim, J. H. Ahn, S. H. Kwon, *J. Am. Ceram. Soc.* **2019**, *102*, 5881.
[22] A. Sharma, V. Longo, M. A. Verheijen, A. A. Bol, W. M. M. Kessels, *J. Vac. Sci. Technol., A* **2017**, *35*, 01B130.
[23] L. P. Bakos, J. Mensah, K. László, B. Parditka, Z. Erdélyi, E. Székely, I. Lukács, Z. Kónya, C. Cserháti, C. Zhou, *J. Mater. Chem. C* **2020**, *8*, 6891.
[24] a) J. F. Conley, Y. Ono, D. J. Tweet, W. Zhuang, R. Solanki, *J. Appl. Phys.* **2003**, *93*, 712; b) H. J. Lee, J. H. Hwang, J.-Y. Park, S. W. Lee, *ACS Appl. Electron. Mater.* **2021**, *3*, 999.
[25] C. B. Musgrave, R. G. Gordon, *Future Fab Int.* **2005**, *18*, 126.
[26] J. H. Park, Y. B. Yoo, K. H. Lee, W. S. Jang, J. Y. Oh, S. S. Chae, H. K. Baik, *ACS Appl. Mater. Interfaces* **2013**, *5*, 410.
[27] Z. Guo, A. Liu, Y. Meng, C. Fan, B. Shin, G. Liu, F. Shan, *Ceram. Int.* **2017**, *43*, 15194.
[28] a) Y. Wang, L. Jiang, Y. Liu, D. Tang, F. Liu, Y. Lai, *J. Alloys Compd.* **2017**, *727*, 469; b) Y. Huang, P. Ruiz, *J. Phys. Chem. B* **2005**, *109*, 22420.
[29] Y. Widjaja, C. B. Musgrave, *J. Chem. Phys.* **2002**, *117*, 1931.
[30] a) Y. Shao, X. Wu, M. N. Zhang, W. J. Liu, S. J. Ding, *Nanoscale Res. Lett.* **2019**, *14*, 122; b) Y. Wu, L. Lan, P. He, Y. Lin, C. Deng, S. Chen, J. Peng, *Appl. Sci.* **2021**, *11*, 4393.
[31] C.-E. Kim, J. M. Skelton, A. Walsh, A. Soon, *J. Mater. Chem. C* **2015**, *3*, 11349.
[32] S. S. Barala, V. S. Bhati, M. Kumar, *Thin Solid Films* **2017**, *639*, 107.
[33] L. Zuo, X. Jiang, L. Yang, M. Xu, Y. Nan, Q. Yan, H. Chen, *Appl. Phys. Lett.* **2011**, *99*, 183306.
[34] a) P. M. Jordan, D. K. Simon, F. P. G. Fengler, T. Mikolajick, I. Dirnstorfer, *Energy Procedia* **2015**, *77*, 91; b) Y. J. Kim, D. Lim, H. H. Han, A. S. Sergeevich, Y.-R. Jeon, J. H. Lee, S. K. Son, C. Choi, *Microelectron. Eng.* **2017**, *178*, 284.
[35] K. Kukli, M. Ritala, T. Sajavaara, J. Keinonen, M. Leskelä, *Thin Solid Films* **2002**, *416*, 72.
[36] a) J. Robertson, B. Falabretti, *Mater. Sci. Eng., B* **2006**, *135*, 267; b) M. Liu, Q. Fang, G. He, L. Li, L. Q. Zhu, G. H. Li, L. D. Zhang, *Appl. Phys. Lett.* **2006**, *88*, 192904.
[37] C. R. Kagan, A. Paul, *Thin-Film Transistors*, CRC Press, New York, NY **2003**.
[38] M. Napari, T. N. Huq, D. J. Meeth, M. J. Heikkila, K. M. Niang, H. Wang, T. Iivonen, H. Wang, M. Leskela, M. Ritala, A. J. Flewitt, R. L. Z. Hoye, J. L. MacManus-Driscoll, *ACS Appl. Mater. Interfaces* **2021**, *13*, 4156.
[39] A. Liu, H. Zhu, Y.-Y. Noh, *Adv. Funct. Mater.* **2020**, *30*, 2002625.
[40] E. Lee, J. Ko, K.-H. Lim, K. Kim, S. Y. Park, J. M. Myoung, Y. S. Kim, *Adv. Funct. Mater.* **2014**, *24*, 4689.
[41] K. Arstila, J. Julin, M. I. Laitinen, J. Aalto, T. Konu, S. Kärkkäinen, S. Rahkonen, M. Raunio, J. Itkonen, J. P. Santanen, *Nucl. Instrum. Methods Phys. Res., Sect. B* **2014**, *331*, 34.